molecules

MDPI

Article

UV and Visible Light-Driven Production of Hydroxyl Radicals by Reduced Forms of N, F, and P Codoped Titanium Dioxide

A. M. Abdullah [1], Miguel Á. Gracia-Pinilla [2], Suresh C. Pillai [3] and Kevin O'Shea [1,*]

[1] Department of Chemistry & Biochemistry, Florida International University, Miami, FL 33199, USA; am.abdullah@fiu.edu

[2] Facultad de Ciencias Físico Matemáticas, Universidad Autónoma de Nuevo León, Av. Universidad s/n, Cd. Universitaria, San Nicolás de los Garza, Nuevo León 66455, Mexico; miguel.graciapl@uanl.edu.mx

[3] Nanotechnology and Bio-engineering Research Group, Department of Environmental Science, Institute of Technology, Sligo F91 YW50, Ireland; pillai.suresh@itsligo.ie

* Correspondence: osheak@fiu.edu; Tel.: +1-305-348-3968

Received: 15 May 2019; Accepted: 3 June 2019; Published: 6 June 2019

Abstract: The photocatalytic activities of reduced titanium dioxide (TiO_2) materials have been investigated by measuring their ability to produce hydroxyl radicals under UV and visible light irradiation. Degussa P25 TiO_2 was doped with nitrogen (N), fluorine (F), and/or phosphorus (P) and then subjected to surface modification employing a thermo-physicochemical process in the presence of reducing agent sodium borohydride ($NaBH_4$). The reduced TiO_2 materials were characterized by a number of X-ray, spectroscopic and imaging methods. Surface doping of TiO_2 was employed to modulate the band gap energies into the visible wavelength region for better overlap with the solar spectrum. Hydroxyl radical generation, central to TiO_2 photocatalytic water purification applications, was quantitated using coumarin as a trap under UV and visible light irradiation of the reduced TiO_2 materials. At 350 nm irradiation, the yield of hydroxyl radicals generated by the reduced forms of TiO_2 was nearly 90% of hydroxyl radicals generated by the Degussa P25 TiO_2. Hydroxyl radical generation by these reduced forms of TiO_2 was also observed under visible light irradiation (419 and 450 nm). These results demonstrated that simple surface modification of doped TiO_2 can lead to visible light activity, which is important for more economical solar-driven applications of TiO_2 photocatalysis.

Keywords: visible light activated titanium dioxide; visible light activated TiO_2; hydroxyl radical; hydroxyl radical quantification; photocatalytic activity; coumarin

1. Introduction

While titanium dioxide (TiO_2) has attracted remarkable attention as a photocatalyst over the past few decades for the treatment of wastewater and the degradation of hazardous chemicals, significant industrial applications and commercial benefits have yet to be realized [1–3]. TiO_2 photocatalysis requires absorption of a photon, typically in the UV region ($\lambda < 400$ nm), to generate an electron (e^-_{CB})/hole(h^+_{VB}) pair, Equation (1), which can initiate degradation through the production of reactive oxygen species (ROS) as outlined below in Equations (1)–(5). The recombination of the electron/hole pair is often a dominant process which eliminates the potential for the formation of ROS. In competition with recombination, the electron/hole pairs can migrate to the surface of TiO_2 and form ROS in the presence of water and oxygen [4–7]. While direct oxidation and reduction of target substrates by electron/hole pair can also be envisioned, such direct transformations are generally not competitive in aqueous solution. The primary processes leading to degradation of target pollutants usually involve

the formation of ROS, hydroxyl radicals (•OH), Equations (2) and (5), superoxide anion radicals ($O_2^{\bullet-}$), Equation (3), and hydrogen peroxide (H_2O_2), Equation (4). Although a number of ROS are generated in a TiO_2 photo-oxidation process and can lead to the mineralization of organic pollutants, hydroxyl radical (•OH) is considered the primary species leading to degradation [8–10].

$$TiO_2 + h\nu \rightarrow h^+_{VB} + e^-_{CB} \quad (1)$$

$$H_2O + h^+_{VB} \rightarrow H^+ + \bullet OH \quad (2)$$

$$O_2 + e^-_{CB} \rightarrow O_2^{\bullet-} \quad (3)$$

$$2H_2O + 2O_2^{\bullet-} \rightarrow H_2O_2 + 2HO\bullet + O_2 \quad (4)$$

$$H_2O_2 + e^-_{CB} \rightarrow 2HO\bullet \quad (5)$$

TiO_2 is readily available, inexpensive, and chemically stable; however, there are two major drawbacks to TiO_2 photocatalysis [3,11]. Firstly, the photo-excitation of unmodified TiO_2 requires UV light. Secondly, the quantum yield for photochemical production of ROS is low due to the rapid recombination of electron/hole pairs [7,12]. The solar spectrum is predominately in the visible region, with only ~5% of the total irradiation in the UV region. A major challenge in TiO_2 photocatalysis is to utilize the visible region of the solar spectrum. Extension of the TiO_2 light absorption profile into the visible light region offers significantly improved economic viability compared to those requiring UV activation. A number of techniques including nonmetal doping with nitrogen (N), sulfur (S), carbon (C), fluorine (F), iodine (I), or boron (B), nonmetal codoping, metal deposition, dye sensitization, semiconductor coupling, and enriching the oxygen content of TiO_2 have led to a variety of visible light activated (VLA) TiO_2 materials over the last decade [1,3,13–20]. A number of metal doping materials has been previously explored; however, metal doping often produces undesirable metal titanates at high processing temperatures [21–24]. Nonmetal doping or codoping into the TiO_2 modifies the valence band level of TiO_2, reducing the effective band gap energy, as shown in Figure 1, and modulating the light absorption into the visible light region [25–30]. Although the incorporation of dopant elements can result in the advantage of narrowing band gap energies, dopants can influence charge carrier recombination processes, and the limited solubility of dopants into the bulk materials as well as thermal instability have limited photocatalytic applications of doped TiO_2 materials [31–35].

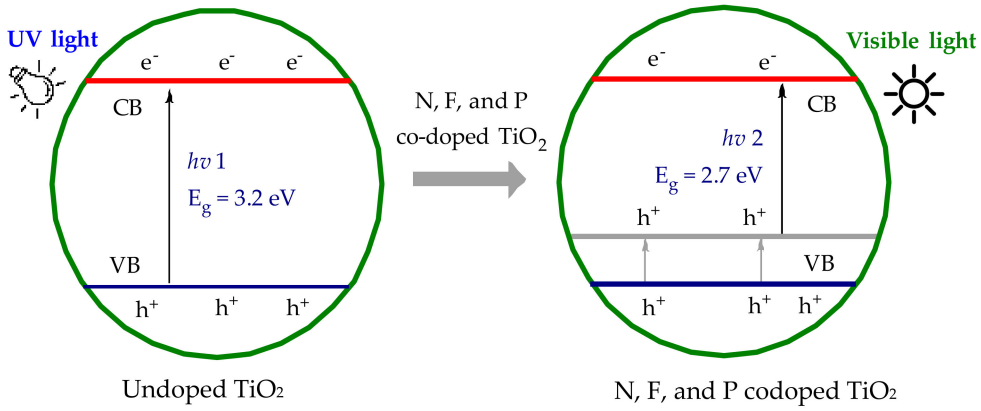

Figure 1. Schematic band gap energy levels of doped and undoped TiO_2; E_g stands for the band energy gap between the valance band (VB) and conduction band (CB).

Simple reduction of Ti within the TiO_2 matrix leads to stable colored TiO_2 with visible light absorbing properties, and these materials have attracted extensive attention due to their enhanced photocatalytic activity [36–39]. Notably, black TiO_2 prepared from the hydrogenation of TiO_2 nanocrystals at high-pressure exhibits relatively low band gap energy and enhanced photocatalytic activity for water splitting and dye degradation [36]. A number of approaches, including high

pressure, high temperature, plasma-assisted hydrogenation, and high-temperature aluminum vapor reduction, have been explored for preparation of VLA TiO_2 materials [37–40]. High-pressure and/or high-temperature protocols are often experimentally challenging and/or expensive. Recently, Tan et al. developed a fast and simple chemical reduction method for the production of colored TiO_2 through a controllable solid-state reaction of $NaBH_4$ and crystalline TiO_2 at moderate temperature (< 300 °C) [41]. The resulting reduced TiO_2 material possessed a narrow band gap with a crystalline core/amorphous shell structure (TiO_2@TiO_{2-x}) containing oxygen vacancies at the surface of TiO_2 promoting the separation of charge carriers and leading to improved VLA photocatalytic performance. Herein, we synthesized reduced codoped P25 TiO_2 through thermal treatment in the presence of $NaBH_4$ in an attempt to extend the TiO_2 photocatalytic function into the visible light region.

Although reduction and codoping of TiO_2 can narrow band gap energies appropriate for the absorption of visible light, enhanced visible light photocatalytic activity is not ensured [3]. The photocatalytic activity is generally associated with a redox reaction initiated by the photogenerated charge carriers. Assessment and comparisons of the photocatalytic activity of different TiO_2 materials are challenging due to the variation of experimental conditions, equipment design, flux intensity, loading, band gap, surface area, and crystal lattice and composition. While the application of TiO_2 photocatalysis for remediation of pollutants and toxins in aqueous media has been studied extensively, assessing the specific effectiveness of the photocatalyst is still not standardized [42–47]. Since •OH is generally the primary species initiating the degradation of target pollutants during TiO_2 photocatalysis, monitoring •OH production during TiO_2 photocatalysis is an effective way to evaluate TiO_2 photocatalytic activity. Noteworthy, Xiang et al. reported an OH-index parameter, as expressed in Equation (6), to assess the activity of a photocatalyst [47].

$$\text{OH-index} = (r/r_0) \times 100 \quad (6)$$

where r and r_0 are the formation rate of •OH on the irradiated photocatalyst and reference photocatalyst P25 TiO_2, respectively. P25 TiO_2 was taken as the reference standard for the production of •OH under UV irradiation as one of the most extensively investigated and most active commercial photocatalysts [46].

Direct measurement of •OH is difficult because its short wavelength absorbance (<230 nm) makes it difficult to monitor and its high reactivity results in an extremely short lifetime (often 10^{-9} s) [10]. Given these limitations, indirect methods have been established to trap hydroxyl radicals with the formation of stable hydroxyl radical adducts. Among hydroxyl radical traps, coumarin (COU) forms a hydroxyl radical adduct which can be readily quantitated using fluorescence spectroscopy. We have employed coumarin which yields 7-hydroxycoumarin (7HC) upon trapping of hydroxyl radical, as shown in Scheme 1. The concentration of 7HC measured by fluorescence is proportional to the production of hydroxyl radicals by TiO_2 materials under UV and visible light [48].

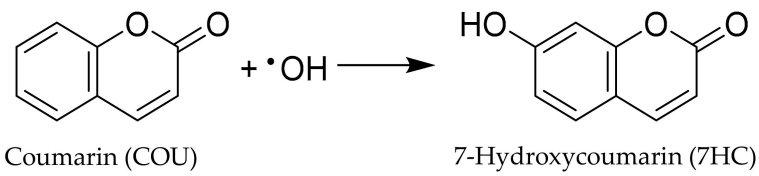

Coumarin (COU) 7-Hydroxycoumarin (7HC)

Scheme 1. The reaction of COU and •OH for highly florescent 7HC production.

One of the purposes of this study was to develop visible light active forms of TiO_2 through a simple reduction process. We prepared the VLA TiO_2 materials using a controllable solid state thermal physicochemical process. Detailed physical and chemical characterization of the prepared materials, along with their optical properties, were carried out by a number of techniques including X-ray powder diffraction (XRD), high-resolution transmission electron microscope (HRTEM), energy dispersive X-ray fluorescence (EDXRF), ultraviolet-visible (UV-Vis) spectroscopy, and Raman spectroscopy. Hydroxyl radical production is reported as a measure of the viability of these TiO_2 materials for the destruction

of environmental contaminants in potential water treatment applications. The study also compares the relative photocatalytic efficiency of prepared TiO_2 materials using OH-index. Our results provide insight into the development of visible light-activated photocatalysts for the destruction of organic pollutants in water.

2. Results and Discussions

A series of reduced TiO_2 materials (identified as TiO_2^{red}) for P25 TiO_2 and N, F, and/or P codoped TiO_2 (NF-TiO_2 and NFP-TiO_2) were synthesized by thermal treatment with $NaBH_4$ for 30, 50, and 70 minfollowing the reported method [41] as detailed in the experimental section. The specific conditions of thermal treatment used in the preparation of reduced TiO_2 materials are tabulated in Table 1, and the optical reflectance of representative samples are shown in Figure 2.

Table 1. The prepared TiO_2 materials as a function of reduction time with $NaBH_4$ along with their thicknesses of the amorphous layer.

Series Name	Treatment Time with $NaBH_4$ at 300 °C					
	30 min	Thickness(nm)	50 min	Thickness (nm)	70 min	Thickness (nm)
P25 TiO_2	$TiO_2^{red\ 30}$	1.2	$TiO_2^{red\ 50}$	1.5	$TiO_2^{red\ 70}$	2.0
NF-TiO_2	NF-$TiO_2^{red\ 30}$	1.3	NF-$TiO_2^{red\ 50}$	2.1	NF-$TiO_2^{red\ 70}$	6.0
NFP-TiO_2	NFP-$TiO_2^{red\ 30}$	1.0	NFP-$TiO_2^{red\ 50}$	1.5	NFP-$TiO_2^{red\ 70}$	2.0

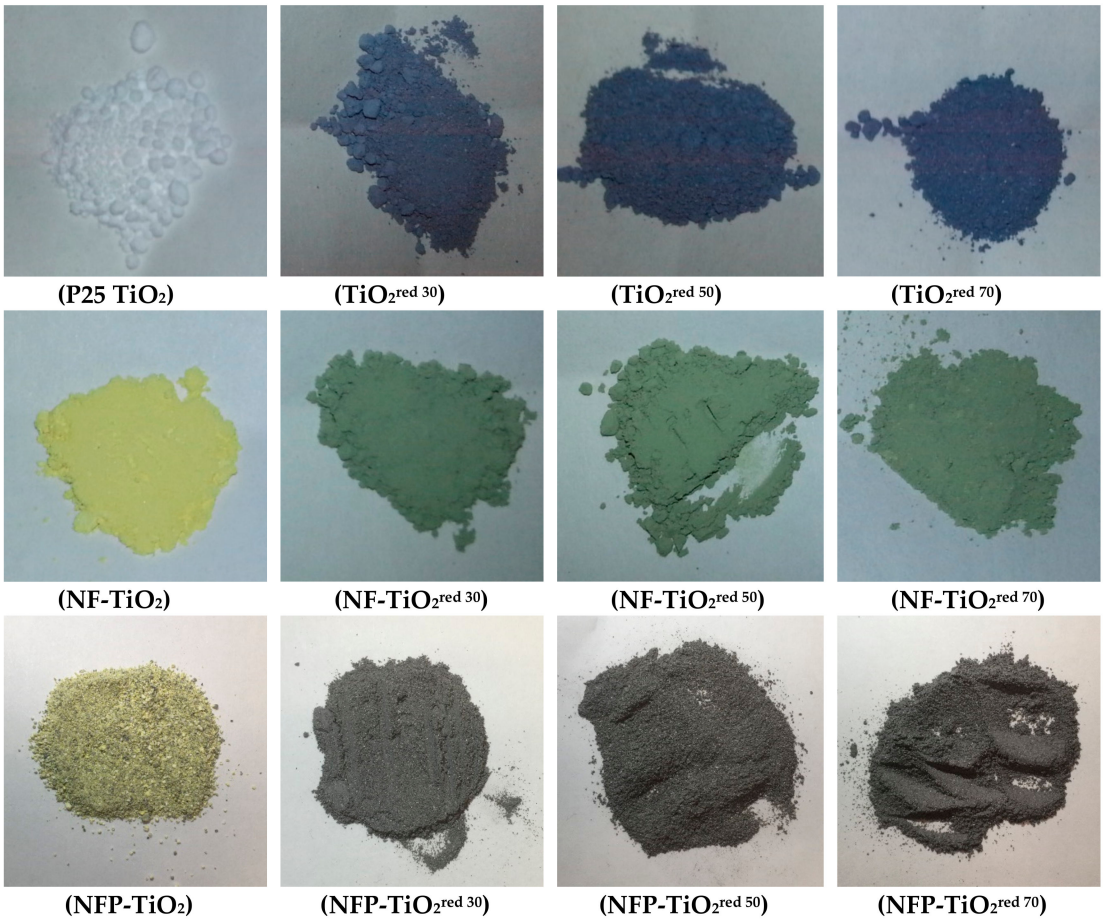

Figure 2. Color photographs of reduced TiO_2 synthesized by thermal treatment with $NaBH_4$.

2.1. Phase Structure Analysis

The performance of a photocatalyst is often dependent on the many factors, including the crystal structure, surface area, and composition [18,22,49]. TiO_2 can exist as three different forms; anatase,

rutile, and brookite [21,49–52]. Anatase is considered the most photocatalytically active crystal form. The photocatalytic activity of TiO_2 can vary dramatically based on its lattice structure, and thus, X-ray powder diffraction (XRD) patterns were used to analyze the crystalline properties of synthesized TiO_2 samples. The XRD data of P25 TiO_2 and reduced TiO_2 are provided in Figure 3. All observed peaks in the XRD patterns of the reference P25 TiO_2 and the reduced TiO_2^{red} were indexed to anatase and rutile phases. The intensity of XRD peaks for $TiO_2^{red\ 70}$ associated with the anatase phase, however, decreased, indicating lower crystallization due to surface modification at longer treatment times without a significant change of crystallinity. Anatase (tetragonal structure, a and b) 3.78 Å; c) 9.50 Å) and rutile (tetragonal structure, a and b) 4.58 Å; c) 2.95 Å) are the two major forms of crystalline TiO_2. Titanium oxide can also exist in another thermodynamically unstable form called brookite (rhombohedral structure, a) 5.43 Å; b) 9.16 Å; c) 5.13 Å). The brookite phase was not detected in any of the samples in this study. Previous experiments showed that anatase is kinetically more stable than rutile while rutile is reported to be more thermodynamically stable than anatase at normal atmospheric pressure and temperature [11,51]. It has been found that a crystalline mixture of the two different phases of titanium dioxide, such as anatase and rutile is more photoactive than 100% anatase [51–53].

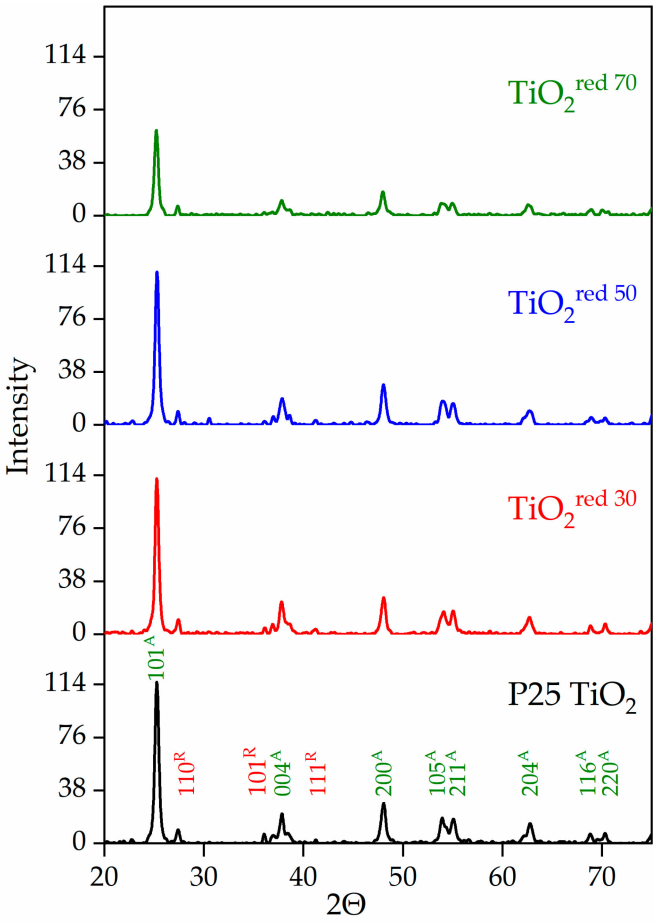

Figure 3. Comparison of XRD patterns among P25 TiO_2 and reduced forms of P25 TiO_2 materials (green and red Millar indices represent the anatase and rutile phases, respectively).

2.2. Microstructural and Morphological Analysis

Micrographs of high-resolution transmission electron microscopy (HRTEM) of P25 TiO_2 materials are presented in Figure 4, while the reduced forms of NF-TiO_2, and NFP-TiO_2 are included in the Supplementary Materials (Figure S1). The high crystalline order of the TiO_2 nanoparticles with the characteristic lattice of anatase possessing indexed planes of (101) and (200) was observed in all

samples. A thin amorphous layer was observed at the surface of the reduced TiO_2 nanoparticles, indicative of surface modification. The measured thicknesses of the amorphous layers are tabulated in Table 1. The values of the amorphous layer and the characteristics of the crystalline order of the anatase suggest that we can modulate the amorphous layer by changing the duration of thermal treatment and consequently modulate the band gap energies into the visible light region.

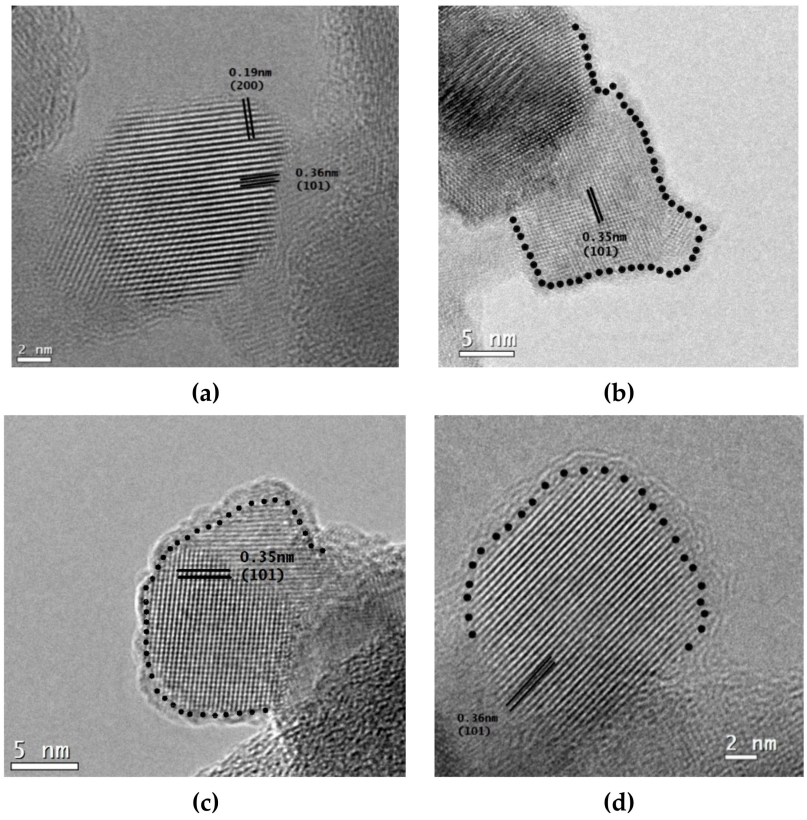

Figure 4. HRTEM images of TiO_2 nanocrystals: (**a**) P25 TiO_2 before reduction, (**b**) $TiO_2^{red\ 30}$ (1.2 nm of the amorphous layer), (**c**) $TiO_2^{red\ 50}$ (1.5 nm of the amorphous layer), and (**d**) $TiO_2^{red\ 70}$ (2.0 nm of the amorphous layer).

2.3. Energy Dispersive X-ray Fluorescence (EDXRF) Analysis

Our results demonstrated effective doping of TiO_2 with nonmetals N, F, and P. Chemical composition as weight percentage for the synthesized catalyst NF-TiO_2 was N (7.17%), O (42.46%), F (3.40%), and Ti (46.97%) and for the NFP-TiO_2 the composition was determined as N (9.17%), O (37.28%), F (12.56%), P (7.35%), and Ti (33.65%). The XRF spectrum of doped samples NF-TiO_2 and NFP-TiO_2 are presented in Supplementary Materials (Figure S2). Degussa P25 has an average crystalline size of 21 nm with a specific surface area of 50 m^2/g [54]. The particle size of 22.3 nm was calculated for the NFP samples processed at 600 °C, with a modest increase to 29.5 nm at 1000 °C and 40.7 nm 1100 °C reported [11].

2.4. Ultraviolet-visible (UV-Vis) and Raman Spectroscopy

The colors of the prepared TiO_2, presented in Figure 2, indicate visible light absorption. The UV-visible diffuse reflectance spectra of the reduced TiO_2 samples, provided in Supplementary Materials (Figure S3), were used to determine the specific absorption edges and band gap energies. The results demonstrated the band gap energies of doped samples shift to the visible light region compared to the unmodified P25 TiO_2. A reduction of the band gap energy from 3.1 eV to 2.23 eV was observed for P25 TiO_2 after treatment for approximately one hour. For NF-TiO_2 particles, the band gap

energy dropped by 0.8 eV to 1.30 eV. The NFP-TiO_2 particles possess a band gap of 2.7 eV, decreasing to 2.35 eV upon reduction. The insertion of N atoms into TiO_2 lattices is reported to create a new interband state above the valence band of TiO_2 leading to the observed absorbance shift into the visible light region [55]. Since the absorbance edges of the prepared samples shifted into the visible light region, we assigned surface modification and production of an amorphous layer on the TiO_2 particle results to changes in the band gap energy and visible light absorption properties. The band gap energies calculated by Kubelka–Munk plots are summarized in Table 2.

Table 2. Band gap of $NaBH_4$ treated P25 TiO_2, NF-TiO_2, and NFP-TiO_2 series and their corresponding photoexcited absorption wavelength.

Particles	ΔE (eV)	λ (nm)	Particles	ΔE (eV)	λ (nm)	Particles	ΔE (eV)	λ (nm)
P25 TiO_2	3.10	400	NF-TiO_2	2.10	590	NFP-TiO_2	2.70	459
$TiO_2^{red\ 30}$	2.40	516	NF-$TiO_2^{red\ 30}$	1.43	867	NFP-$TiO_2^{red\ 30}$	2.51	494
$TiO_2^{red\ 50}$	2.30	540	NF-$TiO_2^{red\ 50}$	1.35	918	NFP-$TiO_2^{red\ 50}$	2.40	516
$TiO_2^{red\ 70}$	2.23	556	NF-$TiO_2^{red\ 70}$	1.30	953	NFP-$TiO_2^{red\ 70}$	2.35	527

Raman spectra of the TiO_2 materials exhibited the characteristic bands corresponding to Eg1, Bg1, Ag1, and Eg3 at 146, 396, 516, and 637 cm-1, respectively (data shown in Supplementary Materials Table S1), for the vibrational modes of the anatase phase of TiO_2 [56]. Small shifts of the vibration mode were observed, as shown in Figure 5. The modest shift is assigned to the surface disorder as a result of the amorphous layer over the TiO_2 nanoparticle (possible formation of oxygen vacancies or nonstoichiometry defects). Amorphous surface layers can also lead to peak broadening. Oxygen vacancy promotes the charge carrier separation and can potentially enhance the photocatalytic performance [41].

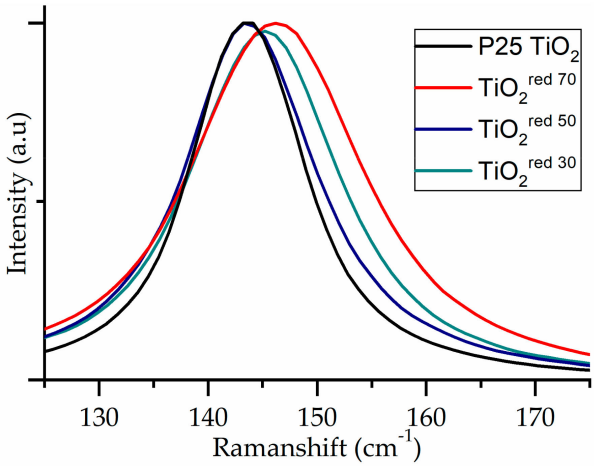

Figure 5. Raman spectrum of P25 TiO_2 series showing shift toward the visible region as a function of reductive treatment time.

2.5. Photocatalytic Hydroxyl Radicals (•OH) Production

The production of the •OH adduct, 7HC, was monitored to assess the production of •OH by the reduced TiO_2 materials at different irradiation wavelengths. Figure 6 shows the growth of fluorescence intensity at 455 nm of the hydroxyl radical trapping agent, 7HC, as a function of irradiation time under 350 UV light in the presence of P25 TiO_2, as a reference for comparing different photocatalysts. Control experiments in the dark and in the absence of P25 TiO_2 did not yield 7HC. The inset of Figure 6 shows the concentration of 7HC in P25 TiO_2 aqueous suspension as a function of irradiation time. Triplicate experiments yielded reproducibility within 95%. The yield of 7HC increased in a linear fashion initially and reached a maximum at approximately 1.0 μM at 20 minof irradiation. Upon

continued irradiation, the production of 7HC gradually decreased due to the likely depletion of coumarin, as well as the simultaneous formation and degradation of 7HC at higher concentrations. The formation of 7HC followed pseudo-zero-order kinetics in accordance with previous reports [46,57]. An apparent pseudo-zero-order rate constant (k_{app}) of 0.16 μM min^{-1} (R^2 = 0.99) was determined under our experimental conditions. The observed rate constant was different from the rate constant of 0.023 μM min^{-1} reported by Nagarajan et al. [46], likely due to differences in experimental conditions including starting concentration, flux intensity, reactor design, etc. The concentration of 7HC (1.0 μM) produced at 20 minwas equivalent to [•OH] = 16.4 μM, assuming trapping efficiency of 6.1% of total •OH [46,57].

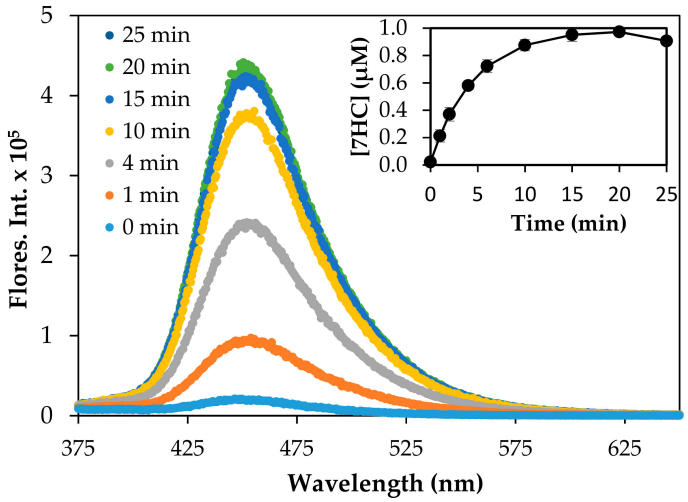

Figure 6. Change of fluorescence intensity observed at 455 nm during the irradiation of P25 TiO_2 (0.10 g/L) suspended in a 125 μM COU aqueous solution. The plot of 7HC vs irradiation time is shown in the inset. The irradiation of P25 TiO_2 suspension was carried out at 350 nm.

2.6. Evaluation of the Photocatalytic Performance

The photocatalytic production of 7HC of the reduced TiO_2 materials was carried out under the same conditions employed for the baseline using P25 TiO_2 irradiation at λ = 350, 419, and 450 nm. Significant amounts of •OH, quantitated based on the formation of 7HC, were produced by reduced P25 TiO_2 under UV (350 nm) irradiation shown in Figure 7. The formation of 7HC by reduced TiO_2^{red} was slower than the reference P25 TiO_2 and followed the order of $TiO_2^{red\ 30}$> $TiO_2^{red\ 70}$> $TiO_2^{red\ 50}$. Under 350 nm, the productions of hydroxyl radicals by reduced, doped NF-TiO_2 and NFP-TiO_2 were insignificant (data shown in Supplementary Materials Figure S4). No direct correlation was observed with the treatment time by $NaBH_4$, •OH production, and the band gap energies.

Visible light-activated photocatalysis has been reported to be effective for the degradation of organic pollutants [13,14,23,54]. The band gap of P25 TiO_2 is 3.1 eV, and upon reduction with $NaBH_4$, the band gap energy decreases to 2.23 eV, corresponding to light absorption wavelengths ~556 nm. Based on the calculated band gap for NF-TiO_2 and NFP-TiO_2 series, shown in Table 2, reduced NF-TiO_2^{red} and NFP-TiO_2^{red} may be active in the near IR region and at ~500 nm, respectively. The photocatalytic production of 7HC in aqueous suspension of the synthesized TiO_2 materials under irradiation at 419 and 450 nm is presented in Figure 8. For quantitative estimation of their relative photocatalytic activity, we calculated OH-index for each of the prepared samples using Equation (6) based on the formation rate of 7HC correlated to the production of •OH for only the initial 10 minof reaction to avoid the possible degradation of 7HC. The calculated OH-indexes are summarized in Table 3. Though the formation rate of •OH depends on various factors, including phase structures, particle size, crystallinity, and surface defects, the composition is an important factor in the photolytic activity of TiO_2 materials. A graphical comparison production of •OH at visible light is presented in Figure 9.

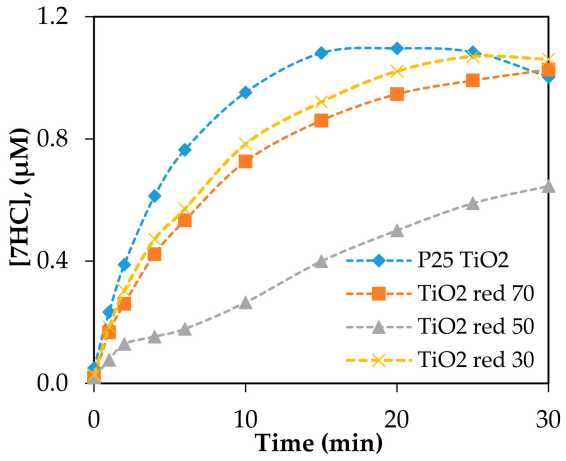

Figure 7. The production of 7HC by reduced P25 TiO_2 photocatalysts irradiated at 350 nm. Catalyst loading was 0.10 g/L; [COU] = 125 μM.

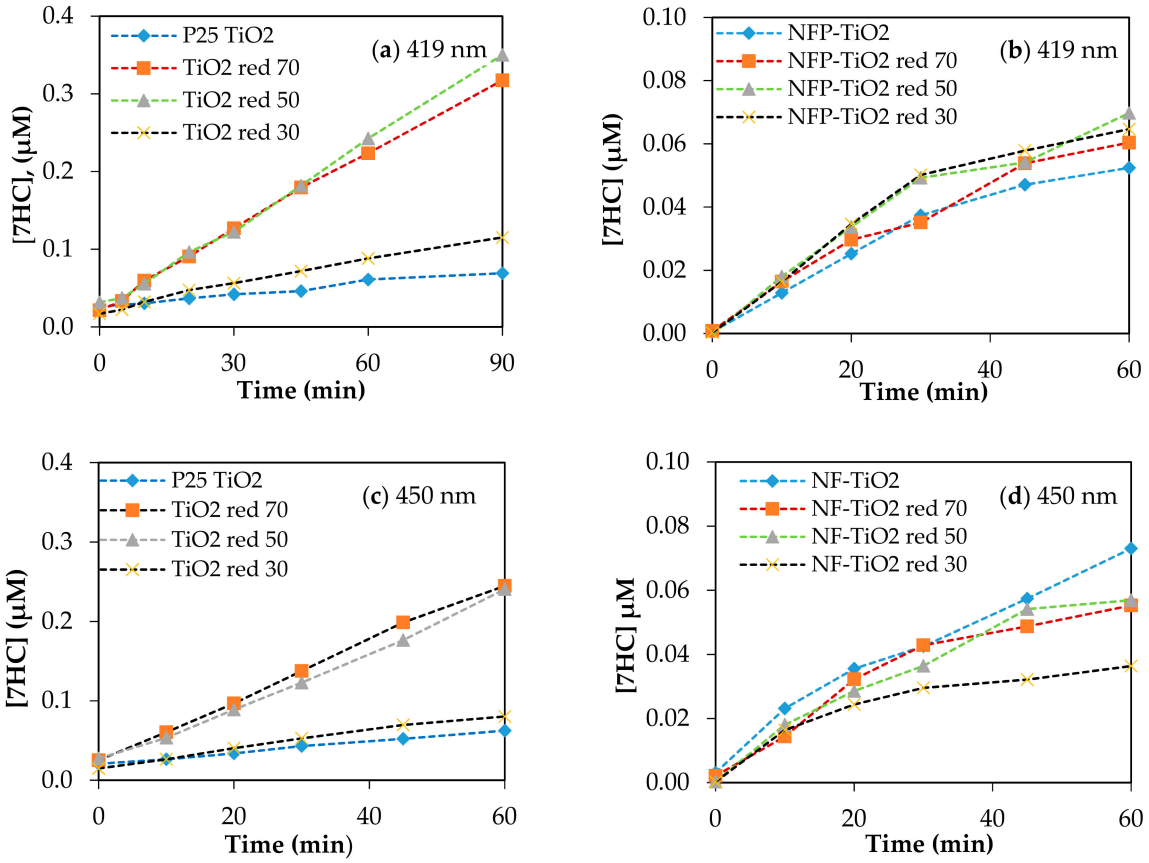

Figure 8. Production of 7HC using various TiO_2 upon irradiation at visible light (**a**,**b**) 419 nm; (**c**,**d**) 450 nm. Catalyst loading was 0.10g/L; [COU] = 125 μM.

In general, the larger the OH-index, the higher the photocatalytic activity. P25 TiO_2 showed the highest OH-index for UV activation compared to the reduced TiO_2 materials. P25 TiO_2 is among the most active photocatalysts for the degradation of organic compounds initiated by •OH radicals under UV irradiation. However, under the visible light region, P25 TiO_2 did not show appreciable photo activity. In the visible range, $NaBH_4$ treated P25 TiO_2, $TiO_2^{red\ 70}$, $TiO_2^{red\ 50}$, and $TiO_2^{red\ 30}$, showed enhanced photocatalytic activity compared to reference P25 TiO_2. Though NFP codoped TiO_2 exhibited limited photocatalytic activity under visible light, $NaBH_4$ treatment did not make a difference in the performance.

Table 3. Calculated OH-index of prepared TiO_2 materials.

Catalysts	OH-index		
	350 nm	419 nm	450 nm
P25 TiO_2	100[A]	0.3	0.4
$TiO_2^{red\ 70}$	86	2.1	2.5
$TiO_2^{red\ 30}$	75	2.2	2.4
$TiO_2^{red\ 50}$	33	0.7	0.7
NF-TiO_2	0.04	n/d	0.8
NF-$TiO_2^{red\ 70}$	0.03	n/d	0.9
NF-$TiO_2^{red\ 50}$	0.06	n/d	0.7
NF-$TiO_2^{red\ 30}$	0.05	n/d	0.6
NFP-TiO_2	0.01	0.8	n/d
NFP-$TiO_2^{red\ 70}$	0.01	0.9	n/d
NFP-$TiO_2^{red\ 50}$	0.01	0.8	n/d
NFP-$TiO_2^{red\ 30}$	0.01	1.1	n/d

[A] The data are reproducible with 5% of error based on some triplicate run. n/d represents no photocatalytic experiment of respective material for this condition was carried out.

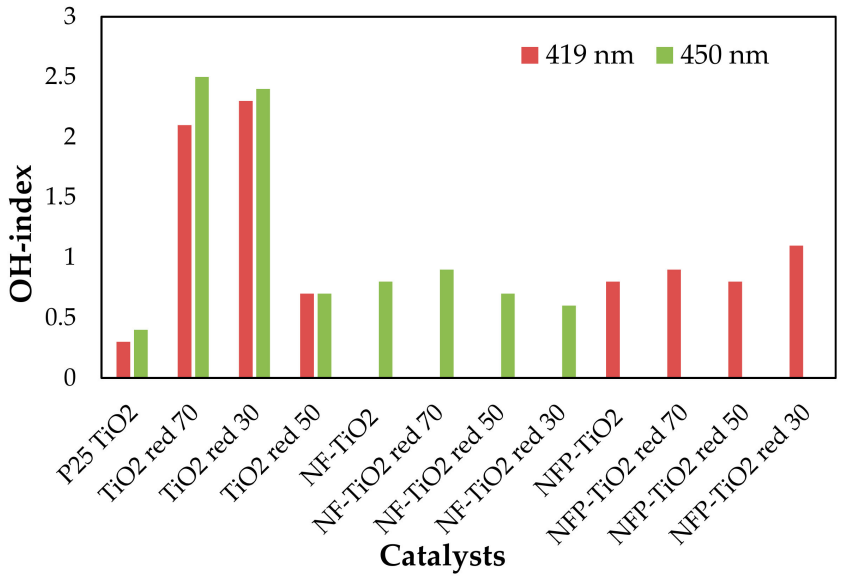

Figure 9. Relative comparison of OH-index of various TiO_2-based photocatalysts at visible light (the data are reproducible with 5% of error based on some triplicate runs).

3. Materials and Methods

3.1. Materials

P25 TiO_2 donated by Degussa was employed as starting material. N and F codoped TiO_2 (NF-TiO_2) and N, F, and P codoped TiO_2 (NFP-TiO_2) were prepared by using titanium tetraisopropoxide (97.0%), isopropanol (99.0%), ammonium hexafluorophosphate (NFP) (≥95.0%), urea (N) (≥98.0%), trifluoroacetic acid (TFA) (99.0%), and phosphoric acid (PA) (85 wt.%) A detailed experimental procedure to prepare these samples is given in Ref [11]. $NaBH_4$ obtained from Acros Organics was 98% pure and used without further purification. Coumarin was purchased from MP Biomedicals, LLC. 7-Hydroxycoumarin (7HC) was 99% pure and purchased from Acros Organics. The air used to purge samples was from Trigas of the highest available purity. Millipore water (18 MΩ·cm) was used for the preparation of all aqueous solutions.

3.2. Preparation of Reduced TiO_2 Materials

In a typical procedure, 4.0 g of P25 TiO_2 was mixed with 1.5 g of $NaBH_4$ in an agate mortar and thoroughly ground with a pestle for 30 minat room temperature. The resulting mixture was transferred to a porcelain boat and placed in a tubular furnace. Gradient heat was applied at a rate of 10 °C min^{-1} from room temperature to 300 °C under an argon atmosphere and baked for an additional 30–70 minat 300 °C. The sample was removed from the furnace and allowed to naturally cool to room temperature. The resulting colored TiO_2 was washed with deionized water and ethanol several times to eliminate unreacted $NaBH_4$ and undesired byproducts. The washed sample was stored for characterization after drying at 70 °C for one hour. A series of reduced forms of NF-TiO_2 (NF-TiO_2^{red}) and reduced forms of NFP-TiO_2 (NFP-TiO_2^{red}) were prepared as a function of reduction time.

3.3. Characterization of Reduced TiO_2 Materials

X-ray diffraction patterns were taken for the reduced TiO_2 materials employing a Bruker Advance D8 X-ray diffractometer, with Cu Kα (λ = 1.54056) radiation with continuous scanning in the range of $10° < 2\Theta < 90°$. Structure, surface morphology, and microstructure of prepared materials were characterized by high-resolution transmission electron microscope (HRTEM) imaging studies using FEI TITAN G2 80–300 operated at 300 kV. Samples were sonicated and placed onto a carbon-coated copper grid for scanning by microscope. The concentration of N, F, P, and Ti in doped TiO_2 samples was determined using the energy dispersive X-ray fluorescence (EDXRF) analyses. The vibrational spectroscopy of hybrid nanostructure was identified using Thermo Scientific XDR Raman microscope employing 532 nm laser at 5 mW power. The UV-Visible absorption spectra of the various TiO_2 materials were recorded at room temperature on a Varian Cary 100 Bio UV-Visible spectrophotometer in the wavelength range of 220–800 nm. The band gap of the prepared samples was calculated from Kubelka–Munk plots.

3.4. Photocatalytic Experiment

The illumination of the TiO_2 suspension was carried out in a Rayonet Photochemical Reactor equipped with a cooling fan and up to 16 lamps in a merry-go-round arrangement (details of the reactor, model RPR-100, are available at The Southern New England Ultra Violet Company [58]. Three sets of lamps provide specific irradiation centered around 350, 419, or 450 nm. Eight lamps equally distributed within the reactor were employed in each experiment. A phosphor-coated black light of nearly 350 nm was used for UV irradiation and white tungsten bulbs of 419 and 450 nm for visible light irradiations. The intensity of light fluxes for 350 nm, 419 nm, and 450 nm was in 10% deviation according to manufacturer specifications. Pyrex glass reaction vessels with Teflon stoppers (L = 30 cm, D = 2.5 cm) were employed for all photocatalysis experiments. In a typical experiment, 100 mL of 125 μM COU aqueous solution was loaded with 10 mg of catalyst and sonicated in an ultrasonic cleaning bath for 10 minto produce a uniform of suspension. The mixture was gently purged with air for 10 minprior to irradiation. The aqueous suspension was magnetically stirred during irradiation in a photochemical reactor. The reaction vessel was removed from the reactor at desired time intervals, vigorously shaken for 30 s, and a 5.0 mL aliquot withdrawn from the reaction solution and immediately passed through a 0.45 μm PTFE filter. The filter was rinsed with another 5.0 ml of deionized water combined with filtrate to make the total volume of 10 ml for future analyses.

3.5. Measurement of the Formation of Hydroxyl Radicals (•OH) for Assessing the Photocatalytic Activities

The concentrations of •OH during irradiation of the aqueous TiO_2 suspensions were measured from the concentration of highly fluorescent hydroxyl radical adduct (7HC) produced from the reaction of •OH with COU. Based on the established yield of 7HC from the COU + •OH reaction, the concentration of •OH production can be determined as a function of irradiation time. The optimal COU concentration ranges for •OH production are reported between 100–1000 μM [12]. Czili et

al. observed maximum initial yields when the COU concentration was 100 μM [48]. While •OH generated during TiO_2 photocatalysis is primarily formed at the surface, $•OH_{ads}$ can diffuse from the TiO_2 surface, leading to free •OH. Previous studies have shown free •OH, and $•OH_{ads}$ occur at or near the surface and have similar reactivities. The trapping efficiency of •OH in TiO_2 suspension reported by Zhang et al. is ~6.1% using 100 μM COU [57]. Newton and Milligan reported similar trapping efficiency of 4.7% [59]. The detection and quantification of 7HC were carried out by a Horiba FluoroMax Spectrofluorometer setting with excitation and emission wavelengths at 332 and 455 nm, respectively. The equipment was calibrated against a series of standard 7HC concentrations ranging from 0.1 to 3.0 μM (0.1, 0.5, 1.0, 1.5, 2.0, and 3.0 μM). The calibration plot, shown in Supplementary Materials (Figure S5) was obtained by plotting the fluorescence intensity measured at 455 nm as a function of 7HC concentration. The correlation coefficient of the calibration plot was ≥ 0.99.

4. Conclusions

The visible light-activated reduced forms of TiO_2 materials were prepared by a simple solid state thermo-physicochemical treatment using $NaBH_4$. The materials were subsequently characterized by XRD, HRTEM, EDXRF, UV-Visible, and Raman spectrometry. Optical measurement suggested that physicochemical treatment can modulate the band gap energy-suitable properties for efficient photocatalytic activity. Coumarin was used as a fluorescent probe to trap and measure the •OH generated in catalyst suspension under UV and visible light irradiation. The photocatalytic performances of the synthesized reduced TiO_2 materials were assessed by quantitative measurement of hydroxyl radical production under the irradiation of UV and visible light. Finally, OH-index of a photocatalyst using the formation rate of hydroxyl radicals was calculated to compare the relative photocatalytic activity of a photocatalyst. Though P25 TiO_2 was found as the most active photocatalyst in the UV region, $NaBH_4$-reduced forms of TiO_2 were identified as significantly active photocatalysts under visible irradiation.

Supplementary Materials: The following are available online at http://www.mdpi.com/1420-3049/24/11/2147/s1, Figure S1a: HRTEM images of NF-TiO_2. Figure S1b: HRTEM images of NFP-TiO_2 nanocrystals, Figure S2: EDXRF spectrum of (a) NF-TiO_2, and (b) NFP-TiO_2, Figure S3: UV-Visible diffuse reflectance spectra of (a) P25 TiO_2 series, (c) NF-TiO_2 series, and (e) NFP-TiO_2 series. The Kubelka-Munk plot for band energy calculation for (b) P25 TiO_2 series, (d) NF-TiO_2 series, and (f) NFP-TiO_2 series, Figure S4: The production of 7HC at 350 nm by (a) reduced NF-TiO_2 and (b) NFP-TiO_2 photocatalyst, Figure S5: Spectrofluorometric calibration curve for measuring of 7HC. Table S1a: Raman band position of P25 TiO_2 and reduced P25 TiO_2 (TiO_2^{red}), Table S1b: Raman band position of NF-TiO_2 and reduced NF-TiO_2^{red}, Table S1c: Raman band position of NFP- TiO_2 and reduced NFP-TiO_2^{red}.

Author Contributions: K.O. made the concept of the project, design of experiments, oversight of data analysis. A.M.A. did the most of experimental work and wrote the report. M.Á.G.-P. did partial experimental work, and S.C.P. was the provider of doped N, F, and/or P codoped TiO_2. All authors discussed the results and commented on the manuscript.

Acknowledgments: Kevin O'Shea acknowledges the National Science Foundation for the partial support of the project (Grant# CHE-1710111). The authors would like to thank Rachel Fagan for helping with sample preparation.

Conflicts of Interest: The authors declare no conflict of interest.

References

1. Daghrir, R.; Drogui, P.; Robert, D. Modified TiO_2 for environmental photocatalytic applications: A review. *Ind. Eng. Chem. Res.* **2013**, *52*, 3581–3599. [CrossRef]
2. Fagan, R.; McCormack, D.E.; Dionysiou, D.D.; Pillai, S.C. A review of solar and visible light active TiO_2 photocatalysis for treating bacteria, cyanotoxins and contaminants of emerging concern. *Mater. Sci. Semicond. Process.* **2016**, *42*, 2–14. [CrossRef]
3. Pelaez, M.; Nolan, N.T.; Pillai, S.C.; Seery, M.K.; Falaras, P.; Kontos, A.G.; Dunlop, P.S.M.; Hamilton, J.W.J.; Byrne, J.A.; O'Shea, K.; et al. A review on the visible light active titanium dioxide photocatalysts for environmental applications. *Appl. Catal. B Environ.* **2012**, *125*, 331–349. [CrossRef]

4. Hoffmann, M.R.; Martin, S.; Choi, W.; Bahnemann, D.W. Environmental applications of semiconductor photocatalysis. *Chem. Rev.* **1995**, *95*, 69–96. [CrossRef]
5. Zhang, J.; Nosaka, Y. Mechanism of the OH radical generation in photocatalysis with TiO_2 of different crystalline types. *J. Phys. Chem. C* **2014**, *118*, 10824–10832. [CrossRef]
6. Dvoranová, D.; Barbieriková, Z.; Brezová, V. Radical intermediates in photoinduced reactions on TiO_2 (An EPR spin trapping study). *Molecules* **2014**, *19*, 17279–17304. [CrossRef] [PubMed]
7. Byrne, C.; Subramanian, G.; Pillai, S.C. Recent advances in photocatalysis for environmental applications. *J. Environ. Chem. Eng.* **2018**, *6*, 3531–3555. [CrossRef]
8. Ollis, D.F.; Pelizzetti, E.; Serpone, N. Photocatalyzed destruction of water contaminants. *Environ. Sci. Technol.* **1991**, *25*, 1522–1529. [CrossRef]
9. Abdullah, A.M.; O'Shea, K.E. TiO_2 photocatalytic degradation of the flame retardant tris (2-chloroethyl) phosphate (TCEP) in aqueous solution: A detailed kinetic and mechanistic study. *J. Photochem. Photobiol. A Chem.* **2019**, *377*, 130–137. [CrossRef]
10. Ishibashi, K.I.; Fujishima, A.; Watanabe, T.; Hashimoto, K. Detection of active oxidative species in TiO_2 photocatalysis using the fluorescence technique. *Electrochem. Commun.* **2000**, *2*, 207–210. [CrossRef]
11. Fagan, R.; McCormack, D.E.; Hinder, S.; Pillai, S.C. Improved high temperature stability of anatase TiO_2 photocatalysts by N, F, P co-doping. *Mater. Des.* **2016**, *96*, 44–53. [CrossRef]
12. Ishibashi, K.; Fujishima, A.; Watanabe, T.; Hashimoto, K. Quantum yields of active oxidative species formed on TiO_2 photocatalyst. *J. Photochem. Photobiol. A Chem.* **2000**, *134*, 139–142. [CrossRef]
13. Zhao, C.; Pelaez, M.; Dionysiou, D.D.; Pillai, S.C.; Byrne, J.A.; O'Shea, K.E. UV and visible light activated TiO_2 photocatalysis of 6-hydroxymethyl uracil, a model compound for the potent cyanotoxin cylindrospermopsin. *Catal. Today* **2014**, *224*, 70–76. [CrossRef]
14. Han, C.; Pelaez, M.; Likodimos, V.; Kontos, A.G.; Falaras, P.; O'Shea, K.; Dionysiou, D.D. Innovative visible light-activated sulfur doped TiO_2 films for water treatment. *Appl. Catal. B Environ.* **2011**, *107*, 77–87. [CrossRef]
15. Pelaez, M.; Falaras, P.; Kontos, A.G.; De la Cruz, A.A.; O'shea, K.; Dunlop, P.S.M.; Byrne, J.A.; Dionysiou, D.D. A comparative study on the removal of cylindrospermopsin and microcystins from water with NF-TiO_2-P25 composite films with visible and UV-vis light photocatalytic activity. *Appl. Catal. B Environ.* **2012**, *121–122*, 30–39. [CrossRef]
16. Byrne, J.A.; Dunlop, P.S.M.; Hamilton, J.W.J.; Fernández-Ibáñez, P.; Polo-López, I.; Sharma, P.K.; Vennard, A.S.M. A review of heterogeneous photocatalysis for water and surface disinfection. *Molecules* **2015**, *20*, 5574–5615. [CrossRef] [PubMed]
17. Ghosh, M.; Liu, J.; Chuang, S.S.C.; Jana, S.C. Fabrication of hierarchical V_2O_5 nanorods on TiO_2 nanofibers and their enhanced photocatalytic activity under visible light. *ChemCatChem* **2018**, *10*, 3305–3318. [CrossRef]
18. Ghosh, M.; Lohrasbi, M.; Chuang, S.S.C.; Jana, S.C. Mesoporous titanium dioxide nanofibers with a significantly enhanced photocatalytic activity. *ChemCatChem* **2016**, *8*, 2525–2535. [CrossRef]
19. Yu, W.; Liu, X.; Pan, L.; Li, J.; Liu, J.; Zhang, J.; Li, P.; Chen, C.; Sun, Z. Enhanced visible light photocatalytic degradation of methylene blue by F-doped TiO_2. *Appl. Surf. Sci.* **2014**, *319*, 107–112. [CrossRef]
20. Adyani, S.M.; Ghorbani, M. A comparative study of physicochemical and photocatalytic properties of visible light responsive Fe, Gd and P single and tri-doped TiO_2 nanomaterials. *J. Rare Earths* **2018**, *36*, 72–85. [CrossRef]
21. Nolan, N.T.; Seery, M.K.; Hinder, S.J.; Healy, L.F.; Pillai, S.C. A systematic study of the effect of silver on the chelation of formic acid to a titanium precursor and the resulting effect on the anatase to rutile transformation of TiO_2. *J. Phys. Chem. C* **2010**, *114*, 13026–13034. [CrossRef]
22. Rajesh Kumar, S.; Pillai, S.C.; Hareesh, U.S.; Mukundan, P.; Warrier, K.G.K. Synthesis of thermally stable, high surface area anatase-alumina mixed oxides. *Mater. Lett.* **2000**, *43*, 286–290. [CrossRef]
23. Seery, M.K.; George, R.; Floris, P.; Pillai, S.C. Silver doped titanium dioxide nanomaterials for enhanced visible light photocatalysis. *J. Photochem. Photobiol. A Chem.* **2007**, *189*, 258–263. [CrossRef]
24. Shakil, M.R.; El-Sawy, A.M.; Tasnim, H.; Meguerdichian, A.G.; Jin, J.; Dubrosky, J.P.; Suib, S.L. Single-doped and multidoped transition-metal (Mn, Fe, Co, and Ni) ZnO and their electrocatalytic activities for oxygen reduction reaction. *Inorg. Chem.* **2018**, *57*, 9977–9987. [CrossRef] [PubMed]
25. McManamon, C.; O'Connell, J.; Delaney, P.; Rasappa, S.; Holmes, J.D.; Morris, M.A. A facile route to synthesis of S-doped TiO_2 nanoparticles for photocatalytic activity. *J. Mol. Catal. A Chem.* **2015**, *406*, 51–57. [CrossRef]

26. Hong, X.; Luo, Z.; Batteas, J.D. Enhanced visible-light absorption and dopant distribution of iodine-TiO_2 nanoparticles synthesized by a new facile two-step hydrothermal method. *J. Solid State Chem.* **2011**, *184*, 2244–2249. [CrossRef]
27. Giannakas, A.E.; Antonopoulou, M.; Deligiannakis, Y.; Konstantinou, I. Preparation, characterization of N–I co-doped TiO_2 and catalytic performance toward simultaneous Cr(VI) reduction and benzoic acid oxidation. *Appl. Catal. B Environ.* **2013**, *140–141*, 636–645. [CrossRef]
28. Zhang, G.; Zhang, Y.C.; Nadagouda, M.; Han, C.; O'Shea, K.; El-Sheikh, S.M.; Ismail, A.A.; Dionysiou, D.D. Visible light-sensitized S, N, and C co-doped polymorphic TiO_2 for photocatalytic destruction of microcystin-LR. *Appl. Catal. B Environ.* **2014**, *144*, 614–621. [CrossRef]
29. Wei, F.; Ni, L.; Cui, P. Preparation and characterization of N–S-codoped TiO_2 photocatalyst and its photocatalytic activity. *J. Hazard. Mater.* **2008**, *156*, 135–140. [CrossRef]
30. Yu, J.; Zhou, M.; Cheng, B.; Zhao, X. Preparation, characterization and photocatalytic activity of in situ N,S-codoped TiO_2 powders. *J. Mol. Catal. A Chem.* **2006**, *246*, 176–184. [CrossRef]
31. Dozzi, M.V.; Selli, E. Doping TiO_2 with p-block elements: Effects on photocatalytic activity. *J. Photochem. Photobiol. C Photochem. Rev.* **2013**, *14*, 13–28. [CrossRef]
32. Abdullah, A.M.; Debnath, T.; Rüscher, C.H.; Hussain, A. Synthesis and characterization of vanadium substituted potassium tungsten bronzes, $K_xV_yW_{1-y}O_3$. *J. Sci. Res.* **2012**, *4*, 507–514. [CrossRef]
33. Yi, Z.; Ye, J.; Kikugawa, N.; Kako, T.; Ouyang, S.; Stuart-Williams, H.; Yang, H.; Cao, J.; Luo, W.; Li, Z.; et al. An orthophosphate semiconductor with photooxidation properties under visible-light irradiation. *Nat. Mater.* **2010**, *9*, 559–564. [CrossRef] [PubMed]
34. Park, J.H.; Kim, S.; Bard, A.J. Novel carbon-doped TiO_2 nanotube arrays with high aspect ratios for efficient solar water splitting. *Nano Lett.* **2006**, *6*, 24–28. [CrossRef] [PubMed]
35. Livraghi, S.; Paganini, M.C.; Giamello, E.; Selloni, A.; Di Valentin, C.; Pacchioni, G. Origin of photoactivity of nitrogen-doped titanium dioxide under visible light. *J. Am. Chem. Soc.* **2006**, *128*, 15666–15671. [CrossRef] [PubMed]
36. Chen, X.; Liu, L.; Yu, P.Y.; Mao, S.S. Increasing solar absorption for photocatalysis with black hydrogenated titanium dioxide nanocrystals. *Science (80-)* **2011**, *331*, 746–750. [CrossRef]
37. Zheng, Z.; Huang, B.; Lu, J.; Wang, Z.; Qin, X.; Zhang, X.; Dai, Y.; Whangbo, M.-H. Hydrogenated titania: synergy of surface modification and morphology improvement for enhanced photocatalytic activity. *Chem. Commun.* **2012**, *48*, 5733–5735. [CrossRef]
38. Naldoni, A.; Allieta, M.; Santangelo, S.; Marelli, M.; Fabbri, F.; Cappelli, S.; Bianchi, C.L.; Psaro, R.; Dal Santo, V. Effect of nature and location of defects on bandgap narrowing in black TiO_2 nanoparticles. *J. Am. Chem. Soc* **2012**, *134*, 7600–7603. [CrossRef]
39. Sinhamahapatra, A.; Jeon, J.-P.; Yu, J.-S. A new approach to prepare highly active and stable black titania for visible light-assisted hydrogen production. *Energy Environ. Sci* **2015**, *8*, 3539–3544. [CrossRef]
40. Wang, Z.; Yang, C.; Lin, T.; Yin, H.; Chen, P.; Wan, D.; Xu, F.; Huang, F.; Lin, J.; Xie, X.; et al. Visible-light photocatalytic, solar thermal and photoelectrochemical properties of aluminium-reduced black titania. *Energy Environ. Sci.* **2013**, *6*, 3007–3014. [CrossRef]
41. Tan, H.; Zhao, Z.; Niu, M.; Mao, C.; Cao, D.; Cheng, D.; Feng, P.; Sun, Z. A facile and versatile method for preparation of colored TiO_2 with enhanced solar-driven photocatalytic activity. *Nanoscale* **2014**, *6*, 10216–23. [CrossRef] [PubMed]
42. Serpone, N.; Sauvé, G.; Koch, R.; Tahiri, H.; Pichat, P.; Piccinini, P.; Pelizzetti, E.; Hidaka, H. Standardization protocol of process efficiencies and activation parameters in heterogeneous photocatalysis: relative photonic efficiencies. *J. Photochem. Photobiol. A Chem.* **1996**, *94*, 191–203. [CrossRef]
43. Serpone, N. Relative photonic efficiencies and quantum yields in heterogeneous photocatalysis. *J. Photochem. Photobiol. A Chem.* **1997**, *104*, 1–12. [CrossRef]
44. Bolton, J.R.; Bircher, K.G.; Tumas, W.; Tolman, C.A. Figures-of-merit for the technical development and application of advanced oxidation technologies for both electric- and solar-driven system (IUPAC technical report). *Pure Appl. Chem* **2001**, *73*, 1998–1999. [CrossRef]
45. Mills, A.; Morris, S. Photomineralization of 4-chlorophenol sensitized by titanium dioxide: a study of the initial kinetics of carbon dioxide photogeneration. *J. Photochem. Photobiol. A Chem.* **1993**, *71*, 75–83. [CrossRef]
46. Nagarajan, S.; Skillen, N.C.; Fina, F.; Zhang, G.; Randorn, C.; Lawton, L.A.; Irvine, J.T.S.; Robertson, P.K.J. Comparative assessment of visible light and UV active photocatalysts by hydroxyl radical quantification. *J. Photochem. Photobiol. A Chem.* **2017**, *334*, 13–19. [CrossRef]

47. Xiang, Q.; Yu, J.; Wong, P.K. Quantitative characterization of hydroxyl radicals produced by various photocatalysts. *J. Colloid Interface Sci.* **2011**, *357*, 163–167. [CrossRef]
48. Czili, H.; Horváth, A. Applicability of coumarin for detecting and measuring hydroxyl radicals generated by photoexcitation of TiO_2 nanoparticles. *Appl. Catal. B Environ.* **2008**, *81*, 295–302. [CrossRef]
49. Byrne, C.; Fagan, R.; Hinder, S.; McCormack, D.E.; Pillai, S.C. New approach of modifying the anatase to rutile transition temperature in TiO_2 photocatalysts. *RSC Adv.* **2016**, *6*, 95232–95238. [CrossRef]
50. Nolan, N.T.; Seery, M.K.; Pillai, S.C. Spectroscopic investigation of the anatase-to-rutile transformation of sol-gel-synthesized TiO_2 photocatalysts. *J. Phys. Chem. C* **2009**, *113*, 16151–16157. [CrossRef]
51. Pillai, S.C.; Periyat, P.; George, R.; McCormack, D.E.; Seery, M.K.; Hayden, H.; Colreavy, J.; Corr, D.; Hinder, S.J. Synthesis of high-temperature stable anatase TiO_2 photocatalyst. *J. Phys. Chem. C* **2007**, *111*, 1605–1611. [CrossRef]
52. Periyat, P.; McCormack, D.E.; Hinder, S.J.; Pillai, S.C. One-pot synthesis of anionic (nitrogen) and cationic (sulfur) codoped high-temperature stable, visible light active, anatase photocatalysts. *J. Phys. Chem. C* **2009**, *113*, 3246–3253. [CrossRef]
53. Banerjee, S.; Pillai, S.C.; Falaras, P.; O'shea, K.E.; Byrne, J.A.; Dionysiou, D.D. New insights into the mechanism of visible light photocatalysis. *J. Phys. Chem. Lett.* **2014**, *5*, 2543–2554. [CrossRef] [PubMed]
54. Nolan, N.T.; Synnott, D.W.; Seery, M.K.; Hinder, S.J.; Van Wassenhoven, A.; Pillai, S.C. Effect of N-doping on the photocatalytic activity of sol-gel TiO_2. *J. Hazard. Mater.* **2012**, *211–212*, 88–94. [CrossRef] [PubMed]
55. Giannakas, A.E.; Seristatidou, E.; Deligiannakis, Y.; Konstantinou, I. Photocatalytic activity of N-doped and N–F co-doped TiO_2 and reduction of chromium(VI) in aqueous solution: An EPR study. *Appl. Catal. B Environ.* **2013**, *132–133*, 460–468. [CrossRef]
56. Cai, J.; Huang, Z.; Lv, K.; Sun, J.; Deng, K. Ti powder-assisted synthesis of Ti^{3+} self-doped TiO_2 nanosheets with enhanced visible light photoactivity. *RSC Adv.* **2014**, *4*, 19588–19593. [CrossRef]
57. Zhang, J.; Nosaka, Y. Quantitative detection of OH radicals for investigating the reaction mechanism of various visible-light TiO_2 photocatalysts in aqueous suspension. *J. Phys. Chem. C* **2013**, *117*, 1383–1391. [CrossRef]
58. The Southern New England Ultraviolet Company Rayonet—Reactors. Available online: https://rayonet.org/reactors.php?part=RPR-100 (accessed on 5 June 2019).
59. Newton, G.L.; Milligan, J.R. Fluorescence detection of hydroxyl radicals. *Radiat. Phys. Chem.* **2006**, *75*, 473–478. [CrossRef]

Sample Availability: Sample Availability: Not available.